Journal of Applied Physics

InAs nano-ridges and thin films grown on (001) silicon substrates

Cite as: J. Appl. Phys. **128**, 035302 (2020); https://doi.org/10.1063/5.0011808
Submitted: 24 April 2020 . Accepted: 03 July 2020 . Published Online: 16 July 2020

Zhao Yan, Yu Han, and Kei May Lau

Journal of Applied Physics ARTICLE scitation.org/journal/jap

InAs nano-ridges and thin films grown on (001) silicon substrates

Cite as: J. Appl. Phys. **128**, 035302 (2020); doi: 10.1063/5.0011808
Submitted: 24 April 2020 · Accepted: 3 July 2020 ·
Published Online: 16 July 2020

Zhao Yan, Yu Han, and Kei May Lau[a)]

AFFILIATIONS

Department of Electronic and Computer Engineering, Hong Kong University of Science and Technology, Clear Water Bay, Kowloon, Hong Kong

[a)]**Author to whom correspondence should be addressed:** eekmlau@ust.hk. **Tel.:** (852)23587049. **Fax:** (852)23581485

ABSTRACT

Monolithic integration of InAs related devices on (001) Si platforms offers potential to extend integrated Si photonics to the mid-infrared (MIR). Here, we systematically studied the hetero-epitaxial growth of in-plane InAs nano-ridges and coalesced thin films on CMOS-standard (001) Si wafers. We started with the growth and optimization of in-plane InAs nano-ridges inside nano-scale Si trenches and developed a three-step growth procedure with a reduced growth rate to obtain uniform InAs nano-ridges with excellent crystalline qualities. We then developed a coalescence process for the optimized InAs nano-ridges to evolve into high quality continuous thin films. In the parametric growth study, we found that a low coalescence rate results in the formation of large InAs islands, while a high coalescence rate promotes the creation of uniform InAs thin films. These InAs/Si templates could serve as virtual substrates for the growth of light emitters and detectors in MIR Si photonics.

I. INTRODUCTION

Extending the application of Si photonics from the near-infrared (NIR) to the mid-infrared (MIR) region could bring additional functionalities beyond data communication onto current Si-based photonics integrated circuits (Si-PIC). Examples include free space communication, light detection/ranging (LIDAR), and gas/bio-sensing.[1–4] The 6.1 Å family of compound semiconductors, namely GaSb, InAs, and their alloys, are ideal candidates for light emission and detection in the MIR region.[5–7] Direct hetero-epitaxy of the 6.1 Å compound semiconductors on (001) Si platforms also provides an economical, scalable, and monolithic integration approach.[8–11] Growing GaSb nanostructures, thin films, and corresponding optoelectronic devices on Si has been extensively researched.[12–15] While quantum cascade lasers were grown on 6° offcut (001) Si substrates,[10] mid-infrared lasers grown on (001) Si with a residual offcut of ~0.5° have also been reported recently.[8,16] Direct epitaxy of high quality InAs thin films on (001) Si remained a challenge due to difficulties in managing the substantial lattice mismatch (11%) and the large diffusion coefficient of indium adatoms.[17–20] As a result, growth of InAs on Si has been limited to nanostructures using selective area growth such as the aspect ratio trapping (ART) and template assisted selective epitaxy (TASE), with GaSb frequently selected as the buffer layer for subsequent InAs growth.[21–25] However, a lattice mismatch of 0.61% between InAs and GaSb could lead to the formation of dislocations when growing thick and fully relaxed InAs.[26–27] Therefore, direct hetero-epitaxy of InAs templates on on-axis (001) Si could produce more integration flexibility for InAs related devices such as 6.1 Å optoelectronic devices as well as future electronic/photonic integrations.[28–31]

The beauty of the ART technique lies at the flexibility in producing both III–V nano-ridges and thin films on (001)-oriented Si wafers, as well as in integrating a variety of III–V optoelectronic devices on Si including transistors, tunneling junctions, lasers, optical amplifiers, and photo-detectors.[32–39] In this work, employing the ART method, we present the direct hetero-epitaxy of InAs nano-ridges and thin films on exact (001)-oriented Si wafers without an intentional miscut angle. We started with the growth of InAs nano-ridges on Si and focused on the optimization of InAs surface morphology via fine-tuning of the growth parameters. Uniform InAs nano-ridge arrays can thus be achieved with a three-step growth procedure at a reduced growth rate of 2 nm/min. To coalesce the nano-ridges into continuous InAs thin films on Si, we found that substantial increase of the growth rate up to 12 nm/min is needed.

Promising crystalline quality was evidenced by cross-sectional transmission electron microscopy (TEM) and high-resolution x-ray diffraction (HRXRD). This study thus provides a viable strategy for the integration of InAs related devices in future MIR Si photonics.

II. EXPERIMENTAL SECTION

Experiments started with the growth of in-plane InAs nano-ridges on pre-patterned on-axis (001) Si substrates. The SiO_2 stripes are oriented toward the [110] direction with 70 nm wide Si openings and 50 nm wide SiO_2 spacers. The thickness of SiO_2 stripes is around 180 nm. The small width of the oxide spacers facilitates the subsequent coalescence of nano-ridges into thin films. Then, V-shaped Si {111} facets were formed by KOH anisotropy wet etching (45% KOH, IPA saturated, 70 °C). We carried out the material growth using a metal-organic chemical vapor deposition (MOCVD) system with a horizontal reactor (AIXTRON 200/4). Triethylgallium (TEGa), trimethylindium (TMIn), and tertiarybutylarsine (TBAs) were used as growth precursors and hydrogen (H_2) as the carrier gas. A thermal cleaning at 800 °C for 15 min to remove native oxide is always used for III–V on Si growth.

A. InAs nano-ridges grown on Si

As shown by the schematic in Fig. 1(a), we started the growth of the InAs nano-ridges using a two-step growth procedure consisting of a 400 °C GaAs nucleation layer with a V/III ratio of 15, followed by the InAs main layer grown at 500 °C with a V/III ratio of 10. The GaAs nucleation layer provides a uniform coverage of the initial {111} Si surface for the subsequent deposition of continuous and uniform InAs nano-ridges, as well as serving as an intermediate buffer to accommodate the large lattice mismatch between InAs and Si. Figure 1(b) presents a tilted scanning electron microscopy (SEM) image of the as-grown InAs nano-ridges inside nano-scale Si trenches. We detected a high density of InAs surface bumps, indicating non-uniform InAs growth inside the Si trenches. We found that the surface morphology can be improved by adopting a lower InAs growth rate. The reduced growth rate provides more time for the deposited InAs to evolve into stable nano-ridge structures with minimum surface energies.[40] As evidenced by the SEM photo in Fig. 1(c), at a low growth rate of 2 nm/min, the density of the surface bumps reduced greatly. As indicated in Fig. 1(c), some surface pits on the InAs stripes were observed. We speculated that the surface pits could stem from the slightly non-uniform GaAs nucleation, which later induces surface pits atop the InAs nano-ridge. We inspected the crystalline quality of the as-grown InAs nano-ridges using cross-sectional TEM. As a result of the defect necking of the ART method and the growth on exposed Si {111} facets, a majority of the defects are confined inside the V-grooved pockets, and the upper part of the InAs nano-ridges exhibit excellent quality without any discernable threading dislocations [Fig. 1(d)]. The InAs nano-ridges develop a convex growth front with two {111} facets, and the shape of the growth fronts varies slightly. Figure 1(e) displays a close-up of the III–V/Si interface. The large lattice mismatch between InAs/GaAs and Si is resolved through the formation of a density of planar defects and a few threading dislocations. We also prepared a TEM specimen along the trench direction as illustrated by the image in Fig. 1(f). As expected, most of the crystalline imperfections are restricted at the III–V/Si interface, while the upper InAs growth is dislocation-free. However, we did observe a few stacking faults propagating up to the nano-ridge surface [white arrow in Fig. 1(f)]. These types of

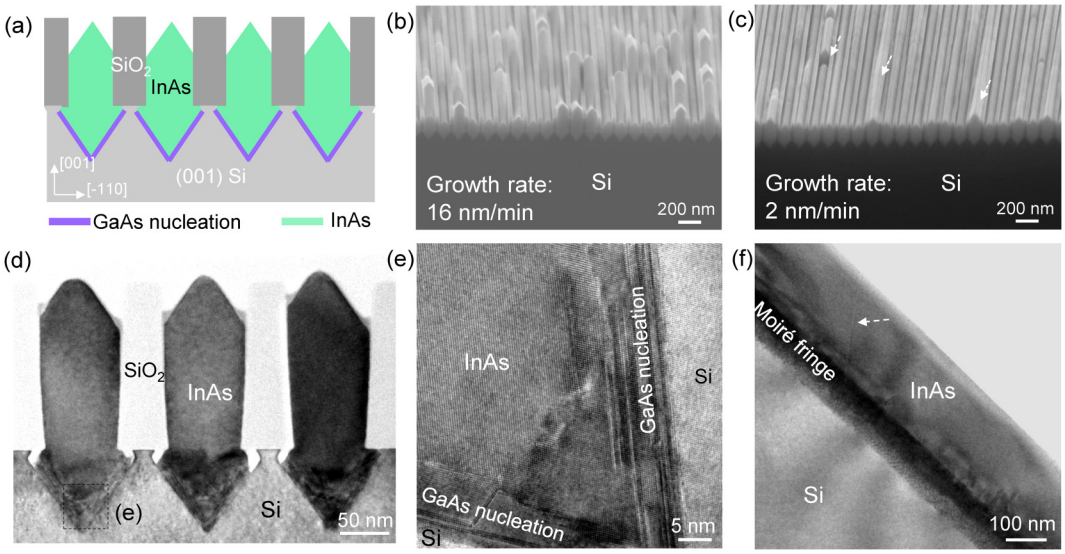

FIG. 1. (a) Schematic of InAs nano-ridges grown on V-grooved Si with a GaAs nucleation layer. (b) InAs bumps formed on the nano-ridges with a fast growth rate. (c) InAs bumps minimized with a slow growth rate. (d) Cross-sectional TEM image of the InAs nano-ridges. (e) High-resolution TEM image of the InAs grown on {111} Si facets with a nucleated GaAs layer. (f) TEM inspection parallel to the nano-ridge direction showing trapped defects at the bottom and one escaped stacking faults.

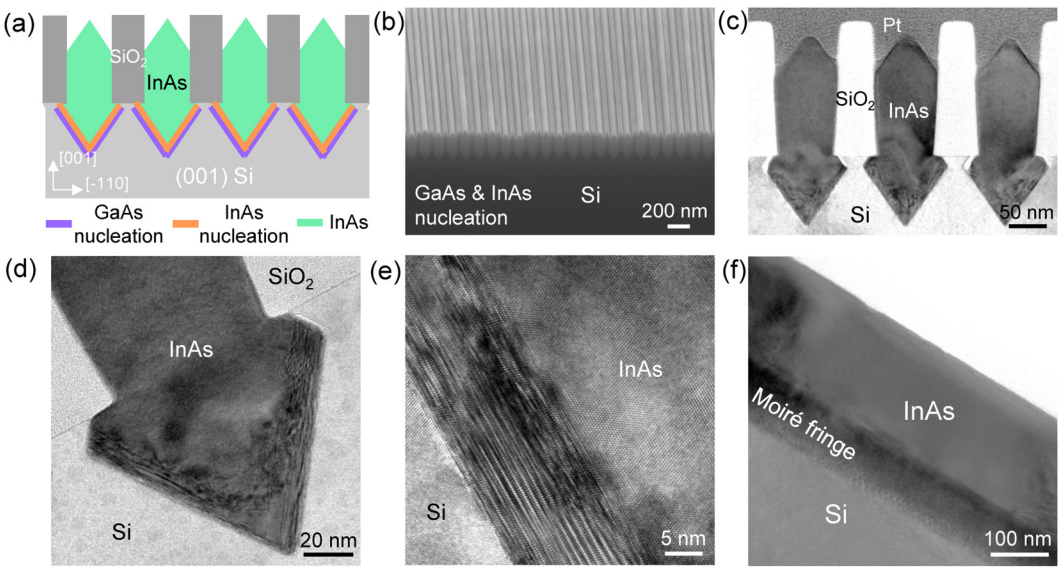

FIG. 2. (a) Schematic illustrating the InAs nano-ridges grown on V-grooved Si with GaAs/InAs double nucleation layer. (b) InAs nano-ridges with uniform morphology. (c) Cross-sectional TEM image of the InAs nano-ridges, and (d) zoomed-in TEM image at the bottom V-groove. (e) High resolution TEM image at the Si boundary to illustrate stacking nucleation layers accommodating the lattice mismatch. (f) TEM inspection parallel to the nano-ridge direction.

stacking faults usually extend to both oxide sidewalls and by no means introduce any partial dislocations inside the nano-ridge crystal.[38]

As a smooth and uniform surface condition of the nano-ridges is a prerequisite for high quality coalesced thin films, we further developed a three-step growth procedure to optimize the nano-ridge morphology. As shown by the schematic in Fig. 2(a), we inserted a thin InAs nucleation layer between the GaAs nucleation and the InAs main layer. The surface morphology of the nano-ridges continues to improve, and we did not observe any surface bumps or pits across the inspected area [SEM photo in Fig. 2(b)]. Figure 2(c) displays a cross-sectional TEM photo of three adjacent InAs nano-ridges. Similarly, most of the defects are restricted within the initial V-grooved pockets, and the nano-ridges exhibit a convex growth front. However, the growth fronts, with two symmetrical {111} facets, are much more uniform with the introduction of the InAs nucleation layer. Figures 2(d) and 2(e) present TEM photos of the V-grooved pocket and reveal the enhanced defect trapping effect. Unlike the sample without InAs layers, in this sample, lattice mismatch was mainly accommodated through the formation of highly twined regions at the III–V/Si interface [zoomed-in TEM photo in Fig. 2(e)]. Figure 2(f) displays a TEM image along the trench direction, with all the crystalline defects confined at the lower part of the InAs.

B. Coalesce InAs nano-ridges into continuous thin films

Building from the optimized InAs nano-ridges with uniform surface morphology and good crystalline quality, we then coalesced the as-grown InAs nano-ridges into continuous InAs thin films. Figure 3 schematically summarizes the growth process of InAs thin films on pre-patterned Si substrates. After growing InAs nano-ridges inside nano-scale Si trenches, we selectively removed the oxide spacers using buffered oxide etch. The closely packed nano-ridges were coalesced into continuous thin films in a regrowth run. Note that, we chose InAs nano-ridges with a reduced ridge height as the seed layer to ease the coalescence process and thus to obtain a smooth surface.[32] We previously employed the same method to grow GaAs, InP, and GaSb thin films on pre-patterned Si substrates.[12,32,41] However, a completely new suite of growth parameters are needed to obtain high quality InAs/Si templates.

Figure 4(a) shows a tilted-view SEM image of the InAs seed layers, revealing a uniform morphology and rhombic-shaped cross sections. To merge the InAs nano-ridges into thin films, a two-step growth procedure similar to GaAs was first attempted. We began the regrowth with coalescing the seed layers using a low growth rate of 1.5 nm/min for 90 min, and then switched to a higher growth rate of 4.5 nm/min to thicken the InAs thin films for 60 min. However, instead of continuous thin films, we observed InAs islands with deep valleys defined by {111} facets, as illustrated by the SEM photo in Fig. 4(b). This feature results from the lowest growth rate of the {111} facets and indicates that {111}-oriented surfaces with minimum surface energies are preferred at this particular growth condition.[42–44] To attain continuous InAs thin films, we modified the InAs regrowth process into a single growth procedure at a high growth rate of 12 nm/min for 30 min. Consequently, we obtained continuous InAs thin films with a top {001}-oriented growth front, as evidenced by the SEM photo in Fig. 4(c). Interestingly, the growth of uniform InAs nano-ridges requires an extremely low growth rate, while the growth of continuous InAs

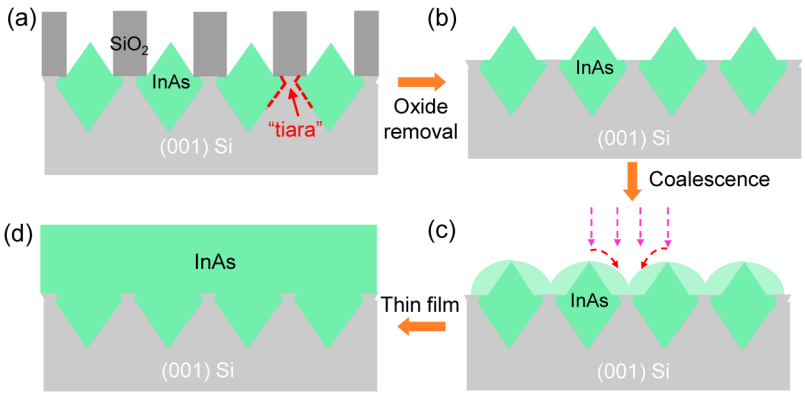

FIG. 3. Schematics summarize the coalescence process of InAs nano-ridges into thin films. (a) InAs nano-ridge as a seed layer. (b) Oxide spacer removal. (c) Coalescence of the InAs nano-ridge seeds by lateral overgrowth. (d) Completion of InAs thin films.

thin films necessitates a high growth rate. We ascribe this discrepancy to the different targeted growth fronts, where the nano-ridges confined by oxide spacers evolve into convex {111}-oriented growth fronts while thin films feature a flat {001}-oriented surface.

We performed cross-sectional TEM to investigate the crystalline quality and defect necking effect of the coalesced InAs thin films. Figure 5(a) shows a zoomed-in TEM photo of the III–V/Si interface, and the dashed lines denote the initial InAs nano-ridge seeds. Lattice mismatch is largely accommodated via the formation of highly twined regions at the interface, and these planar defects are subsequently stopped by the unique "tiara" structures. As indicated in Fig. 5(a), the "tiara" structure consisting of four symmetrical {111} Si facets was formed during the anisotropic KOH wet etch.[32] Apart from the two large {111} facets, two tiny inverted {111} Si facets were also formed from the minor Si undercut [see Fig. 3(a)]. Planar defects along the V-groove surfaces are thereby blocked by these inverted {111} Si facets. Similar "tiara" structures could also be observed in Figs. 1(d) and 2(d). Figure 5(b) displays a global-view TEM image of the InAs thin films, with the TEM lamella prepared perpendicular to the initial nano-ridge direction. This unique coalescence technique results in confinement of crystalline defects mainly within the V-grooved pockets, and the majority of the InAs thin film exhibits a clean morphology. However, we still detect one threading dislocation at the top of the InAs thin film. This type of threading dislocation is probably generated from the III–V/Si interfaces, glides along {111}-planes perpendicular to the nano-ridge direction, and eventually reaches the sample surface. Figure 5(c) presents a global-view TEM photo of the InAs thin films, with the TEM lamella prepared parallel to the initial nano-ridge direction. As expected, the majority of the InAs thin film is clean with most defects restricted at regions close to the III–V/Si interface. But we also observe one stacking fault escaping the confinement of the "tiara" structure and propagating to the sample surface [Fig. 5(c)]. The key to obtain high quality InAs thin film is to enlarge the "tiara" to completely trap the planar defects parallel to the trench direction and to preclude the formation of defects perpendicular to the trench direction through fine-tuning the growth parameters.

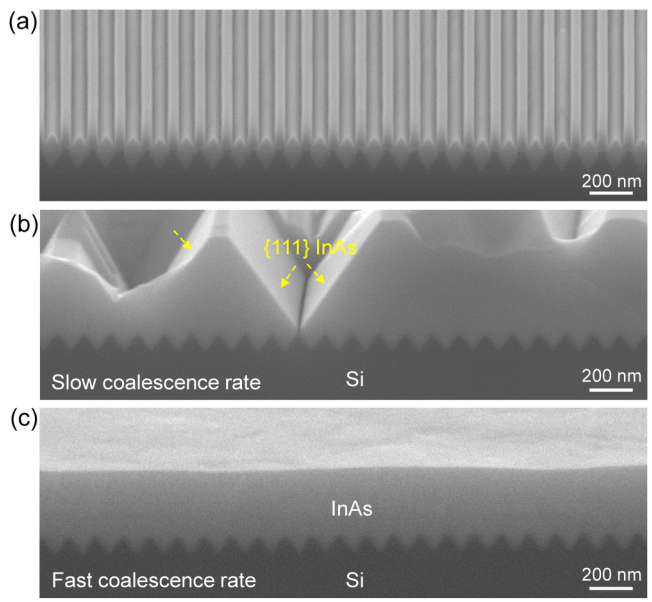

FIG. 4. (a) SEM image of the uniform InAs nano-ridge seed array for lateral coalescence. (b) InAs islands formed with the enclosure of {111} InAs facets if applying at a slow coalescence rate. (c) InAs thin films formed with a fast coalescence rate.

We also carried out high resolution x-ray diffraction (HRXRD) measurements to further evaluate the crystalline quality of the InAs films directly grown on Si. Figure 6(a) plots the ω–2θ curves of 200 nm thick InAs nano-ridges, 450 nm thick InAs thin films, and 1.0 μm thick InAs thin films grown on (001) Si substrates. As the InAs thickens, the diffraction intensity strengthens, the full-width-at-half-maximum (FWHM) reduces, and the peak position gradually moves closer to the Si peak. We extract the FWHM and relaxation percentages of the InAs peaks with different thicknesses and summarize the results in Fig. 6(b). The FWHM of the epitaxial InAs progressively reduces from 424 arcsec to 82 arcsec when the thickness increases from 200 nm to 1 μm. The InAs nano-ridges feature a relaxation percentage of 97%. The slight compressive strain stems from the direct epitaxy on Si substrates as well as the growth confinement inside the Si trenches. The 400 nm thick InAs thin film

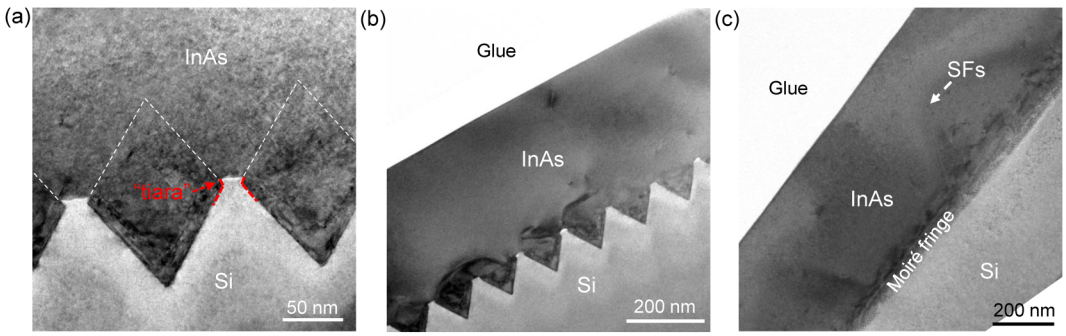

FIG. 5. (a) TEM inspection at the lateral over-growth region showing no additional coalesced defects formed. Planar defects were blocked by the inverted Si {111} facets. (b) and (c) Global-view TEM inspection of InAs thin films along perpendicular and parallel to the nano-ridge direction.

is almost fully relaxed (99.7%). When the film thickness increases up to 1.0 μm, the thermal mismatch between InAs and Si comes into play and induces a slight tensile strain (100.6%) inside the epitaxial InAs thin film. After full relaxation, the strain remains unchanged when we further increase the film thickness to 1.5 μm. A shoulder of the InAs main peak in the XRD measurement was also detected as indicated in Fig. 6(a). It was originated from a slightly different relaxation of the InAs confined inside the Si V-grooves. Other than the InAs and Si peaks, the GaAs nucleation layer also contributed a tiny peak in the middle of the XRD scan [indicated in Fig. 6(a)]. We also performed ω-rocking scans of InAs thin films with different thickness and plot the curves in Fig. 6(c). As the film thickness increases from 450 nm to 1.5 μm, the FWHM of the InAs peaks shrinks from 620 arcsec to 341 arcsec. Based on Ayer's model, the defect density can be estimated by $D \approx \beta^2/(4.36b^2)$,[45] where β is the FWHM of ω-rocking curve in radians and b is the magnitude of Burgers' vector (for 60° dislocation, $b = a/\sqrt{2} = 4.2839$ Å and $a = 6.0583$ Å is the lattice constant of InAs). Therefore, the dislocation density for the 450 nm, 1 μm, and 1.5 μm InAs could be estimated to be $1.13 \times 10^9\,\mathrm{cm}^{-2}$, $7.28 \times 10^8\,\mathrm{cm}^{-2}$, and $3.42 \times 10^8\,\mathrm{cm}^{-2}$, respectively. These values are comparable to those of GaAs thin films grown on planar Si substrates and are far better than those of InP thin films grown on Si with similar thicknesses,[46] despite the significantly larger lattice mismatch between InAs and Si. We attribute the

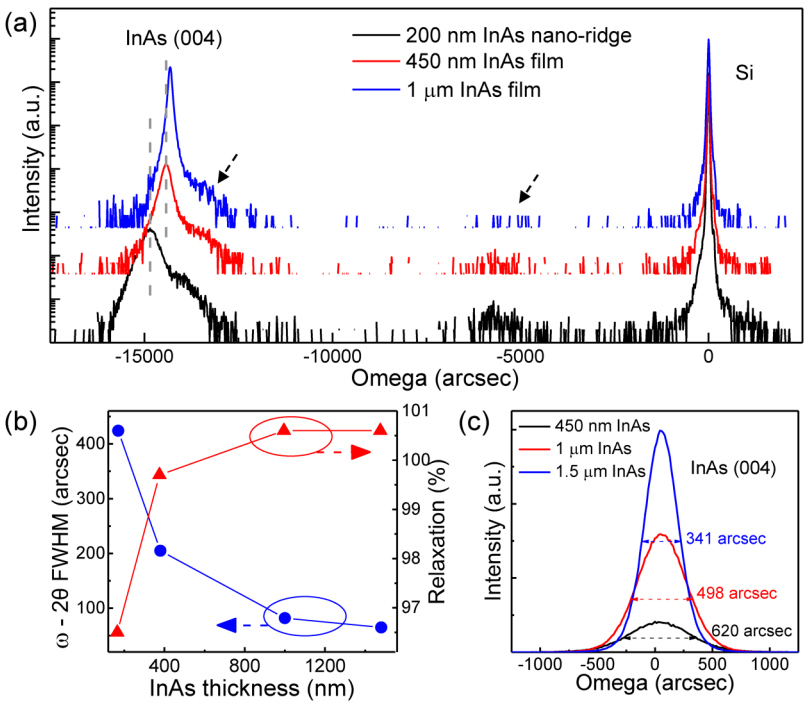

FIG. 6. (a) HRXRD ω–2θ curve of the InAs nano-ridges and thin films indicating the aligned Si peak and slightly mis-aligned InAs peak. (b) Relaxation percentage and FWHM extracted from the InAs peak of the ω–2θ curves. (c) XRD ω-rocking curve of InAs films with different thicknesses.

excellent quality of the InAs thin films to the effective defect necking effect of the ART technique and our optimized growth parameters for InAs hetero-epitaxy on Si.

III. CONCLUSIONS

In conclusion, we have demonstrated the direct growth of InAs nano-ridges and continuous thin films on industry-standard (001) Si substrates. Uniform InAs nano-ridges with excellent crystalline quality were obtained through a three-step growth procedure and adopting a low growth rate. InAs/Si templates were subsequently achieved through coalescing the closely packed nano-ridges into continuous thin films with an elevated growth rate. Our results here suggest the potential of monolithically integrating InAs related light emitters and detectors onto current MIR Si photonics.

AUTHORS' CONTRIBUTIONS

Z.Y. and Y.H. contributed equally to this work

ACKNOWLEDGMENTS

This work was supported in part by the Research Grants Council of Hong Kong (Grant No. 16245216) and in part by the Innovation Technology Fund of Hong Kong (Grant No. ITS/273/16FP). The authors would like to thank the MCPF of HKUST for technical support. Helpful discussions with C. W. Tang are also acknowledged.

DATA AVAILABILITY

The data that support the findings of this study are available from the corresponding author upon reasonable request.

REFERENCES

[1]V. M. Lavchiev and B. Jakoby, IEEE J. Sel. Top. Quantum Electron. **23**, 452 (2017).
[2]T. Hu, B. Dong, X. Luo, T. Y. Liow, J. Song, C. Lee, and G. Q. Lo, Photonic Res. **5**, 5 (2017).
[3]G. Roelkens, U. Dave, A. Gassenq, N. Hattasan, C. Hu, B. Kuyken, F. Leo, A. Malik, M. Muneeb, E. Ryckeboer, S. Uvin, Z. Hens, R. Baets, Y. Shimura, F. Gencarelli, B. Vincent, R. Loo, J. V. Campenhout, L. Cerutti, J. Rodriguez, E. Tournié, X. Chen, M. Nedeljkovic, G. Mashanovich, L. Shen, N. Healy, A. C. Peacock, X. Liu, R. Osgood, and W. Green, Opt. Mater. Express **3**, 9 (2013).
[4]D. Jung, J. Norman, M. J. Kennedy, C. Shang, B. Shin, Y. Wan, A. C. Gossard, and J. E. Bowers, Appl. Phys. Lett. **111**, 122107 (2017).
[5]D. M. Razeghi and B. M. Nguyen, Rep. Prog. Phys. **77**, 082401 (2014).
[6]S. D. Sifferman, H. P. Nair, R. Salas, N. T. Sheehan, S. J. Maddox, A. M. Crook, and S. R. Bank, IEEE J. Sel. Top. Quantum Electron. **21**(6), 1502410 (2015).
[7]D. Jung, S. Bank, M. L. Lee, and D. Wasserman, J. Opt. **19**, 123001 (2017).
[8]M. R. Calvo, L. M. Bartolomé, M. Bahriz, G. Boissier, L. Cerutti, J. B. Rodriguez, and E. Tournié, Optica **7**, 263–266 (2020).
[9]R. Go, H. Krysiak, M. Fetters, P. Figueiredo, M. Suttinger, X. M. Fang, A. Eisenbach, J. M. Fastenau, D. Lubyshev, A. W. K. Liu, N. G. Huy, A. O. Morgan, S. A. Edwards, M. J. Furlong, and A. Lyakh, Opt. Express **26**, 22389–22393 (2018).
[10]H. N. Van, A. N. Baranov, Z. Loghmari, L. Cerutti, J. B. Rodriguez, J. Tournet, G. Narcy, G. Boissier, G. Patriarche, M. Bahriz, E. Tournié, and R. Teissier, Sci. Rep. **8**, 7206 (2018).
[11]R. Go, H. Krysiak, M. Fetters, P. Figueiredo, M. Suttinger, J. Leshin, X. M. Fang, J. M. Fastenau, D. Lubyshev, A. W. K. Liu, A. Eisenbach, M. J. Furlong, and A. Lyakh, Appl. Phys. Lett. **112**, 031103 (2018).
[12]Q. Li, B. Lai, and K. M. Lau, Appl. Phys. Lett. **111**, 172103 (2017).
[13]T. Orzali, A. Vert, B. O'Brian, J. L. Herman, S. Vivekanand, S. S. P. Rao, and S. R. Oktyabrsky, J. Appl. Phys. **120**, 085308 (2016).
[14]Y. Mols, J. Bogdanowicz, P. Favia, P. Lagrain, W. Guo, H. Bender, and B. Kunert, J. Appl. Phys. **125**, 245107 (2019).
[15]M. Baryshnikova, Y. Mols, Y. Ishii, R. Alcotte, H. Han, T. Hantschel, and B. Kunert, Crystals **10**, 330 (2020).
[16]Z. Loghmari, J. B. Rodriguez, A. N. Baranov, M. Rio-Calvo, L. Cerutti, A. Meguekam, M. Bahriz, R. Teissier, and E. Tournié, APL Photonics **5**, 041302 (2020).
[17]Z. M. Zhao, O. Hulko, T. S. Yoon, and Y. H. Xie, J. Appl. Phys. **98**, 123526 (2005).
[18]H. W. Yu, T. M. Wang, H. Q. Nguyen, Y. Y. Wong, Y. Y. Tu, and E. Y. Chang, J. Vac. Sci. Technol. B **32**, 050601 (2014).
[19]S. G. Ghalamestani, M. Berg, K. A. Dick, and L. E. Wernersson, J. Cryst. Growth **332**, 12–16 (2011).
[20]R. Alcotte, M. Martin, J. Moeyaert, P. Gergaud, S. David, T. Cerba, F. Bassani, F. Ducroquet, Y. Bogumilowicz, and T. Baron, Thin Solid Films **645**, 119–123 (2018).
[21]C. W. Hsu, Y. F. Chen, and Y. K. Su, ECS J. Solid State Sci. Tech. **1**(3), P140–P143 (2012).
[22]C. W. Hsu, Y. F. Chen, and Y. K. Su, Nanoscale Res. Lett. **7**, 642 (2012).
[23]M. Borg, H. Schmid, J. Gooth, M. D. Rossell, D. Cutaia, M. Knoedler, N. Bologna, S. Wirths, K. E. Moselund, and H. Riel, ACS Nano. **11**(3), 2554–2560 (2017).
[24]B. M. Borg, K. A. Dick, B. Ganjipour, M. E. Pistol, L. E. Wernersson, and C. Thelander, Nano Lett. **10**, 4080–4085 (2010).
[25]Z. Yan, Y. Han, and K. M. Lau, Nanotechnology **31**, 345707 (2020).
[26]B. R. Bennett, Appl. Phys. Lett. **73**, 3736 (1998).
[27]R. M. Iutzi and E. A. Fitzgerald, J. Appl. Phys. **115**, 234503 (2014).
[28]A. N. Baranov and R. Teissier, IEEE J. Sel. Top. Quantum Electron. **21**, 85 (2015).
[29]S. J. Maddox, W. Sun, Z. Lu, H. P. Nair, J. C. Campbell, and S. R. Bank, Appl. Phys. Lett. **101**, 151124 (2012).
[30]M. Holland, M. V. Dal, B. Duriez, R. Oxland, G. Vellianitis, G. Doornbos, A. Afzalian, T. K. Chen, C. H. Hsieh, P. Ramvall, T. Vasen, Y. C. Yeo, and M. Passlack, Sci. Rep. **7**, 14632 (2017).
[31]W. K. Loke, K. H. Tan, S. Wicaksono, and S. F. Yoon, MRS Commun. **8**, 1085–1091 (2018).
[32]Q. Li, K. W. Ng, and K. M. Lau, Appl. Phys. Lett. **106**, 072105 (2015).
[33]B. Kunert, W. Guo, Y. Mols, B. Tian, Z. Wang, Y. Shi, D. Van Thourhout, M. Pantouvaki, J. Van Campenhout, R. Langer, and K. Barla, Appl. Phys. Lett. **109**, 091101 (2016).
[34]Q. Li, Y. Han, X. Lu, and K. M. Lau, IEEE Electron Device Lett. **37**(1), 24–27 (2016).
[35]Y. Han, Q. Li, S. P. Chang, W. D. Hsu, and K. M. Lau, Appl. Phys. Lett. **108**, 242105 (2016).
[36]Y. Shi, Z. Wang, J. V. Campenhout, M. Pantouvaki, W. Guo, B. Kunert, and D. V. Thourhout, Optica **4**, 12 (2017).
[37]Y. Han, W. K. Ng, C. Ma, Q. Li, S. Zhu, C. C. S. Chan, K. W. Ng, S. Lennon, R. A. Taylor, K. S. Wong, and K. M. Lau, Optica **5**, 8 (2018).
[38]Y. Han, Z. Yan, W. K. Ng, Y. Xue, K. S. Wong, and K. M. Lau, Optica **7**, 148–153 (2020).
[39]Y. Xue, Y. Han, Y. Wang, Z. Zhang, H. K. Tsang, and K. M. Lau, Opt. Lett. **45**, 1754–1757 (2020).
[40]Y. N. Guo, J. Zou, M. Paladugu, H. Wang, Q. Gao, H. H. Tan, and C. Jagadish, Appl. Phys. Lett. **89**, 231917 (2006).
[41]Q. Li, K. W. Ng, C. W. Tang, K. M. Lau, R. Hill, and A. Vert, J. Cryst. Growth **405**, 81–86 (2014).

[42]Y. Han, Q. Li, K. W. Ng, S. Zhu, and K. M. Lau, Nanotechnology **29**, 225601 (2018).
[43]G. Biasiol, A. Gustafsson, K. Leifer, and E. Kapon, Phys. Rev. B **65**, 205306 (2002).
[44]S. Jiang, C. Merckling, W. Guo, N. Waldron, M. Caymax, W. Vandervorst, M. Seefeldt, and M. Heyns, J. Appl. Phys. **115**, 023517 (2014).
[45]J. E. Ayers, J. Cryst. Growth **135**, 71–77 (1994).
[46]B. Shi, Q. Li, and K. M. Lau, J. Appl. Phys. **123**, 193104 (2018).